



UNIVERSITY OF LEEDS

This is a repository copy of *A NIR-II-emitting gold nanocluster-based drug delivery system for smartphone-triggered photodynamic theranostics with rapid body clearance*.

White Rose Research Online URL for this paper:

<https://eprints.whiterose.ac.uk/178909/>

Version: Accepted Version

---

**Article:**

Kong, Y, Santos-Carballal, D [orcid.org/0000-0002-3199-9588](https://orcid.org/0000-0002-3199-9588), Martin, D et al. (11 more authors) (2021) A NIR-II-emitting gold nanocluster-based drug delivery system for smartphone-triggered photodynamic theranostics with rapid body clearance. *Materials Today*, 51. pp. 96-107. ISSN 1369-7021

<https://doi.org/10.1016/j.mattod.2021.09.022>

---

© 2021 Elsevier Ltd. This manuscript version is made available under the CC-BY-NC-ND 4.0 license <http://creativecommons.org/licenses/by-nc-nd/4.0/>.

**Reuse**

This article is distributed under the terms of the Creative Commons Attribution-NonCommercial-NoDerivs (CC BY-NC-ND) licence. This licence only allows you to download this work and share it with others as long as you credit the authors, but you can't change the article in any way or use it commercially. More information and the full terms of the licence here: <https://creativecommons.org/licenses/>

**Takedown**

If you consider content in White Rose Research Online to be in breach of UK law, please notify us by emailing [eprints@whiterose.ac.uk](mailto:eprints@whiterose.ac.uk) including the URL of the record and the reason for the withdrawal request.



[eprints@whiterose.ac.uk](mailto:eprints@whiterose.ac.uk)  
<https://eprints.whiterose.ac.uk/>

## Supplementary Material

---

### **A NIR-II-emitting gold nanocluster-based drug delivery system for smartphone-triggered photodynamic theranostics with rapid body clearance**

Yifei Kong<sup>a</sup>, David Santos-Carballal<sup>b</sup>, David Martin<sup>b</sup>, Natalia N. Sergeeva<sup>b</sup>, Weili Wang<sup>b\*</sup>, Guishi Liu<sup>a</sup>, Benjamin Johnson<sup>c</sup>, Brijesh Bhayana<sup>a</sup>, Zuantao Lin<sup>a</sup>, Yensheng Wang<sup>a</sup>, Xavier Le Guével<sup>d\*</sup>, Nora H de Leeuw<sup>b,e,f</sup>, Dejian Zhou<sup>b\*</sup>, Mei X. Wu<sup>a\*</sup>

<sup>a</sup>Wellman Center for Photomedicine,  
Massachusetts General Hospital,  
Harvard Medical School,  
Boston, MA 02114, United States  
E-mail: [mwu5@mg.harvard.edu](mailto:mwu5@mg.harvard.edu)

<sup>b</sup>School of Chemistry,  
University of Leeds,  
Leeds, LS2 9JT, United Kingdom  
E-mail: [ml07ww@leeds.ac.uk](mailto:ml07ww@leeds.ac.uk); [d.zhou@leeds.ac.uk](mailto:d.zhou@leeds.ac.uk)

<sup>c</sup>School of Physics and Astronomy,  
University of Leeds,  
Leeds, LS2 9JT, United Kingdom

<sup>d</sup>Institute for Advanced Biosciences,  
Université Grenoble-Alpes,  
INSERM U1209,  
CNRS UMR 5309,  
Allée des Alpes,  
38700 La Tronche, France  
E-mail: [xavier.le-guevel@univ-grenoble-alpes.fr](mailto:xavier.le-guevel@univ-grenoble-alpes.fr)

<sup>e</sup>School of Chemistry,  
Cardiff University,  
Cardiff CF10 3AT, United Kingdom

<sup>f</sup>Department of Earth Sciences,  
Utrecht University,  
Budapestlaan 4, 3584 CD Utrecht, The Netherlands

## **Materials and method**

### *Chemical reagents*

Gold(III) chloride hydrate ( $\text{HAuCl}_4 \cdot 3\text{H}_2\text{O}$ ), sodium hydroxide ( $\text{NaOH}$ ), sodium borohydride ( $\text{NaBH}_4$ ), dimethyl sulfoxide (DMSO), 1,2,3-Indantrione monohydrate (ninhydrin), hexylamine, deuterium oxide ( $\text{D}_2\text{O}$ ), 9,10-Anthracenediyl-bis(methylene)dimalonic acid (ABDA), dibenzocyclooctyne-PEG4-N-hydroxysuccinimidyl (DBCO-PEG4-NHS) ester, acridine orange solution (2% in  $\text{H}_2\text{O}$ ) and propidium iodide solution (1.0 mg/mL in  $\text{H}_2\text{O}$ ) were purchased from Sigma-Aldrich. IR-26 dye was ordered from Photonic Solutions. Miniprotein Min-23 ( $M_w$ : ~2340; 99.6 wt.% purity) was synthesized by Shanghai Science Peptide Biological Technology Co. Ltd and GenScript Biotech Co. Ltd. 2',7'-dichlorofluorescein diacetate (DCFDA) cellular reactive oxygen species detection assay kit was ordered from Abcam. All chemicals were used as received without further purification. Ultrapure water with a resistivity of ~18.2  $\text{m}\Omega/\text{cm}$  at 25 °C was used in the preparation of aqueous solutions.

### *Instrumentation*

Water was purified by a Milli-Q water system (Millipore Corporation). Microwave-assisted reactions proceeded in a 10 mL vial within a Biotage Initiator microwave synthesizer (Biotage AB). Buffers were exchanged by dialysis using a Slide-A-Lyzer cassette (2K or 10K MWCO, Thermo Scientific). Centrifugations were carried out in a Heraeus Fresco 21 microcentrifuge (Thermo Scientific). Absorption spectra were recorded on a LAMBDA 950 UV/Vis/NIR spectrophotometer (PerkinElmer). Transmission electron microscopy (HR-TEM) was performed using a FEI Tecnai G2 F20 field emission gun TEM microscope operated at 200 kV and fitted with an 80  $\text{mm}^2$  Oxford Instruments X-Max Silicon Drift Detector (SDD) and a Gatan Orius SC600A CCD camera. NIR-II fluorescence spectra were acquired on a FLS 980 fluorescence spectrometer

(Edinburgh Instruments). Dynamic light scattering (DLS) measurements were carried out at a fixed scattering angle of 90° on a Brookhaven light scattering system (BI-200SM Laser Light Scattering Goniometer) with a BI-APD detector using a He-Ne laser at 633 nm. Zeta potential (ZP) was measured with a Malvern Zetasizer Nano ZS90 analyzer. Cellular DIC and fluorescence images were captured using a Zeiss Axiophot epi-fluorescent microscope. Intracellular ROS levels were quantified in a SpectraMax microplate reader (Molecular Devices). Flow cytometry was analyzed using a FACS Calibur™ system (BD Bioscience). X-ray photoelectron spectra (XPS) were obtained on a Perkin-Elmer PHI 5000C ESCA system with Al K $\alpha$  radiation (1486.6 eV). <sup>1</sup>H NMR spectra were acquired on a Bruker Ultrashield 300 MHz spectrometer and analyzed using Topspin 2.1 software. The amount of Au element in mouse blood, urine and feces was monitored using Agilent 7900 inductively coupled plasma-mass spectrometry (ICP-MS). iPhone 8 Plus's flash was used as the light source for PDT, where the iOS app "Flashlight Timer - Timed Torch" was programmed to switch on and off the flash at the scheduled times. NIR-II *in vivo* fluorescence imaging was performed by a Series III 900/1700 small animal imaging system equipped with an InGaAs camera and an 808 nm excitation laser (Suzhou NIR-Optics Technological Co., Ltd., China). Animal experiments were carried out following NIH guidelines and approved by the local animal ethics committee of CAS.

#### *Microwave synthesis of NIR-II-emitting AuNCs*

A precursor solution was prepared by mixing 1 mL of 25 mg/mL Min-23 with 1 mL of 10 mM HAuCl<sub>4</sub> under vigorous stirring. The solution pH was basified to ~11 by adding 60  $\mu$ L of 1 M NaOH. Afterwards, 20  $\mu$ L of 20 mM NaBH<sub>4</sub> was drop-wisely added with agitation. Of note, the solutions were kept in an ice bath. Immediately thereafter, the mixture was transferred into a 10 mL vial and loaded into a microwave reactor for 1 min heating at 70°C with an input power of 100

W. The resultant solution was dialyzed against PBS (20 mM sodium phosphate, 150 mM sodium chloride, pH 7.4, 500 mL×3) with Slide-A-Lyzer™ cassettes (3.5K MWCO) for the removal of excess reagents and then stored at 4°C in darkness.

### *Computational methods*

Density functional theory (DFT) simulations of the energies, structures and electronic properties of the  $\text{Au}_{25}(\text{SCH}_2\text{CHNH}_2\text{COOH})_{18}$  cluster are investigated. All calculations were performed employing the Vienna *Ab-Initio* Simulation Package (VASP).<sup>1-4</sup> The Kohn-Sham valence electronic states were expanded *via* a periodic plane-wave basis set with a kinetic energy cut-off of 400 eV. The projector augmented wave (PAW) method<sup>5,6</sup> was used for the core (Au: [Xe] 4f<sup>14</sup>; S: [Ne]; O, N, C: [He]) states, their kinetic energy and their interactions with the valence electrons. For the H atoms, the electron was considered as valence. The non-spherical contributions to the gradient of the density were also applied to the PAW spheres, which is important for a proper simulation of the Au *d* electrons when using the meta generalized gradient (meta-GGA) approximation. The method of Grimme D2 was used to enhance the description of the long-range dispersion forces.<sup>7</sup> The calculations were performed using the strongly constrained and appropriately normed (SCAN) exchange-correlation meta-GGA functional.<sup>8</sup> The atomic positions were fully relaxed using an efficient force-based conjugate-gradient method that uses a Newton's line optimizer until the Hellmann-Feynman forces on all ions were less than 0.05 eV Å<sup>-1</sup>.<sup>9,10</sup> The Broyden charge density mixer was allowed to reset after reaching 60 steps, by removing the 5 oldest vectors and reusing the approximation of the charge dielectric function from the previous ionic step, to enhance the electronic convergence during relaxations. The high Fourier components were removed from the projection operators, which were evaluated in real space, *via* a fully automatic optimization. A preconditioned conjugate-gradient algorithm was used for the electronic

minimization. All calculations were performed sampling only the  $\Gamma$  point in the reciprocal space. The partial occupancies were determined using the Gaussian smearing method,<sup>11</sup> with a width set at 0.1 eV. These criteria allowed the convergence of the total energy within  $10^{-5}$  eV per atom.

Static calculations of the clusters were performed to obtain the electronic properties. A Bader partition of the atomic charges was carried out by integrating this quantity within regions with zero flux of electronic density.<sup>12-14</sup> The Bader analysis was performed using as reference the electron density containing the correct total core charge. To simulate the symmetrized electronic properties correctly, firstly we carried out a self-consistent calculation with symmetrization of the charge density, which was followed by a recalculation of the unsymmetrized partial charge density. All structures were drawn using the Visualization for Electronic and Structural Analysis (VESTA) code.<sup>15</sup>

#### *Tissue penetration of NIR-II fluorescence with tissue phantoms*

1) Intralipid®: A plain glass capillary was dipped in Min-23@AuNC (or IR-26) solution (100  $\mu\text{g}/\text{mL}$ ) and transferred to a Petri dish. Both were placed in the NIR-II *in vivo* imaging system for the observation under excitation by an 808 nm laser source (150  $\text{mW}/\text{cm}^2$ , 200 ms exposure, long-pass filter: 1000 nm). After that, 1% Intralipid® medium was added to the dish with the height starting at 1 mm and increased by 1 mm per imaging until 6 mm.

2) Pork muscle: 50  $\mu\text{L}$  of Min-23@AuNC (or IR-26) solution (100  $\mu\text{g}/\text{mL}$ ) was injected into one side of a pork muscle tissue at four different depths *i.e.* 0.5, 1, 1.5 and 2.0 cm beneath the surface. Immediately afterwards, the tissue was placed in the imaging system for taking NIR-II images under the 808 nm laser excitation (150  $\text{mW}/\text{cm}^2$ , 200 ms exposure, long-pass filter: 1000 nm).

#### *Quantification of amine functional groups with Ninhydrin assay*

A 0.35% (*w/v*) ninhydrin solution was freshly prepared by dissolving 350 mg of ninhydrin in 100 mL of absolute ethanol (EtOH). Using serial dilutions, hexylamine standards were prepared with varying concentrations. Thereafter, 200  $\mu\text{L}$  of ninhydrin solution was added to 800  $\mu\text{L}$  of the hexylamine standard and 800  $\mu\text{L}$  of the sample solution (diluting 10  $\mu\text{L}$  of Min-23@AuNCs with 790  $\mu\text{L}$  of distilled water), followed by 40 min incubation at 65°C in a digital dry bath. When the heating was completed, the absorbance of resultant solution at 588 nm was measured and plotted against amine concentration with a linear function.

#### *Synthesis of 2-azido-3-methyl-8-(N,N-dimethylamino)phenazine*

Neutral Red diazonium tetrafluoroborate salt has been synthesized in the accordance with our previously reported procedure.<sup>16</sup> To a solution of Neutral Red diazonium tetrafluoroborate salt (0.010 mmol, 35 mg) in water (10 mL), sodium azide (0.12 mmol, 8.0 mg) in 0.5 mL of water was added and left stirring for 10 min. After no gas evolution was seen, the vessel was sealed and left to stir for 24 h. The reaction was extracted with DCM ( $2 \times 50$  mL) and dried over  $\text{MgSO}_4$ . The residue was concentrated in vacuum and the sample was stored in the freezer. Yield: 7 mg (25%).

#### *Synthesis of NR@Min-23@AuNCs through Cu-free click chemistry*

Crosslinker solution was freshly prepared by dissolving DBCO-PEG4-NHS ester (50 mM) in dry DMSO. Under conjugation, 50  $\mu\text{L}$  of the crosslinker was incubated with 2 mL of Min-23@AuNCs at room temperature (RT) for 1 h. The reaction was stopped by adding 50  $\mu\text{L}$  of quenching buffer (1 M Tris-HCl, pH 8.0) and the resultant solution was dialyzed against PBS. Instead of throwing the dialysates away, they were collected for measuring the absorbance at 307 nm of unreacted crosslinkers (extinction coefficient of DBCO  $\epsilon_{\text{max}} = 12,000 \text{ M}^{-1}\cdot\text{cm}^{-1}$ ), and the binding efficiency was calculated to be ~65%. Thereafter, 200  $\mu\text{L}$  of 25 mM NR dissolved in DMSO was added to 2 mL of DBCO-activated Min-23@AuNC solution. The mixture was incubated at RT for 4 h and

dialyzed against PBS for purification. The absorbance at 452 nm of unreacted NR was measured ( $\epsilon_{\max} = 27,500 \text{ M}^{-1}\cdot\text{cm}^{-1}$ ), and the binding efficiency was ~21%. The resultant DBCO-PEG4@Min-23@AuNCs and NR@Min-23@AuNCs were thoroughly purified by repeated dialysis with Slide-A-Lyzer dialysis cassettes (2K MWCO) against ultrapure water before freeze-drying. For  $^1\text{H}$  NMR measurement, the lyophilized powder was dissolved in deuterated DMSO (DMSO- $d_6$ ), resulting in a solution of 600  $\mu\text{L}$  for each sample.

#### *Cytotoxicity testing*

GES and 4T1 cell lines were successively passaged thrice and separately seeded on two 96-well microplates ( $2.0 \times 10^4$  cells per well). Thereafter, NR@Min-23@AuNCs were added to the designated wells with the final concentration of 0, 10, 50, 100, and 200  $\mu\text{g}/\text{mL}$  and incubated with the cells for 24 h before cytotoxicity testing. Cell viability was determined by standard MTT assay. For easy comparison, the concentrations of Min-23@AuNCs, NR@Min-23@AuNCs and “full-load” NR@Min-23@AuNCs mentioned in the context were based on their Au content.

#### *In vivo systemic toxicity study*

The flow chart (Fig. S19) gives the overall picture of experimental design. Healthy BALB/c mice (age: 6 weeks; weight: 20 g) were randomized into four groups ( $n = 5$  per group). The animals in Group A received no treatment and were used as the control, whilst the others in Groups B, C and D were exposed to 200  $\mu\text{L}$  of NR@Min-23@AuNCs (6.6 mg/Kg) on Day 0. The mice were euthanized with prior bleeding for blood tests on Day 0 (Group A), Day 1 (Group B), Day 3 (Group C) or Day 7 (Group D), after which hearts, livers, intestines, lungs, kidneys, stomachs, brains, spleens and bones were harvested for hematoxylin and eosin (H&E) staining. It is particularly worthwhile to mention that taking repeated blood samples from the same mouse at short intervals (say 3 withdrawals a week) is not applicable under our experimental conditions (Mindray BC-

2800Vet hematology analyzer for blood routine testing; Seamaty SMT-120 chemistry analyzer for biochemistry testing), because the minimum volume (at least 200  $\mu\text{L}$  per time-point) required at each blood test is >10% of total blood volume, which will result in the unattainable recovery of blood components before the following test.<sup>17</sup> For this reason, the mice were exsanguinated for a sufficient amount (~450  $\mu\text{L}$ ) of blood.

The blood samples were analyzed immediately after collecting 16 different types of routine biochemical indicators (Fig. S20). The counts of white blood cell and lymphocyte in the peripheral blood of the mice after exposure to NR@Min-23@AuNCs for 1 day and 3 days show almost one-fold increase in comparison to that of the mice in Group A, which exceed the upper limits of normal range. It is not uncommon that the body releases more white blood cells, especially lymphocytes (the most predominant subset), as a result of the immune response to a foreign substance invasion.<sup>18</sup> However, the measured values fall within the normal ranges on Day 7, where the difference between Group A and Group D is not statistically significant. The results suggest that NR@Min-23@AuNCs were rapidly eliminated from the body and therefore both indicators returned to normal. On the contrary, the mean values of other indicators fluctuate within normal limits for all groups with a few outliers occurring by accident for urea and glucose, which are not associated with the injection of NR@Min-23@AuNCs. The mouse appearance and behavior were assessed through the observation of various parameters (*e.g.*, activity level, body condition, food intake, skin, fur, *etc.*) and no abnormalities were discovered. In addition, there were negligible differences in histology between the control and experimental groups (Fig. S21). Therefore, there are conclusive reasons to believe that NR@Min-23@AuNCs are highly biocompatible.

*AuNC-induced production of singlet oxygen ( $^1\text{O}_2$ )*

ABDA was used to probe the formation of  $^1\text{O}_2$  in solution. 41 mg of ABDA was dissolved in 10 mL of DMSO to prepare the stock solution (10 mM). 100  $\mu\text{L}$  of Min-23@AuNCs (1 mg/mL) was diluted with 895  $\mu\text{L}$  of  $\text{D}_2\text{O}$ , to which 5  $\mu\text{L}$  of ABDA was then added to obtain the final concentration ( $C_f$ ) of 50  $\mu\text{M}$ . After that, the mixture was continuously irradiated under green laser irradiation (532 nm, 100 mW) for 30 min and the UV/vis absorption was recorded every 10 min.

#### *Temperature measurement*

A thermal imaging camera (FLIR ONE Gen 3) was attached on iPhone to measure temperature variation throughout a 2-hour (*in vitro*) or 60-min (*in vivo*) irradiation period. In the *in vitro* study, 2 mL of NR@Min-23@AuNCs (100  $\mu\text{g}/\text{mL}$ ) was added to a well of a 6-well culture microplate, and thereafter thermal images were captured at pre, 1 h and 2 h after continuous irradiation with the smartphone's torch. In order to judge whether NR@Min-23@AuNCs interacted with the light produce heat *in vivo*, 4T1 tumor-bearing mice were randomized into three groups with three mice per group receiving respectively: (I) no treatment (control), (II) irradiation alone, (III) irradiation plus *i.v.* injection of 200  $\mu\text{L}$  NR@Min-23@AuNCs (6.6 mg/Kg). The mice were anesthetized with ketamine/xylazine and exposed to the irradiation without covering the body.

#### *In vitro smartphone-based PDT*

4T1 cells were plated on six 96-well microplates with  $2.0 \times 10^4$  cells per well and incubated for 24 h before PDT treatment. After that, fresh DMEM, Min-23@AuNCs ( $C_f$ : 100  $\mu\text{g}/\text{mL}$ ) or NR@Min-23@AuNCs ( $C_f$ : 100  $\mu\text{g}/\text{mL}$ ) was inoculated in parallel (3 wells per sample) into the designated wells of each plate. Three microplates in top-stage incubators were illuminated by the smartphone's torch (fluence rate: 8  $\text{mW}/\text{cm}^2$ ) for 30 min, among which one microplate was wrapped by aluminum foil with a hole in the center of each well. Meanwhile, other three microplates were maintained in the dark in a  $\text{CO}_2$  incubator. Thereafter, the cells cultured in a

light-illuminated microplate and a dark-kept microplate were stained with DCFDA for the detection of intracellular ROS levels on a microplate reader. The cells cultured in the foil-wrapped microplate and a dark-kept microplate were stained with AO and PI for the observation of cell viability.<sup>18</sup> The cells in two remaining microplates were harvested for quantitative flow cytometric analysis.

#### *In vivo NIR-II imaging and plasma pharmacokinetics*

BALB/c mice at 8 weeks of age, weighing 20 - 25 g, were used for the experiments. 4T1 breast tumor mouse model was established by subcutaneously injecting 100  $\mu$ L of 4T1 cell suspension ( $1 \times 10^6$  cells) into the axillary area or back hind leg of mice. NR@Min-23@AuNCs re-suspended in PBS was intravenously injected to the mice with a dose of 30 mg/kg when the tumors reached 200 - 500 mm<sup>3</sup>. Based on caliper measurement, tumor volume was calculated using the following formula:

$$\text{Tumor volume} = \frac{\pi}{6} (\text{Length} \times \text{Width}^2)$$

Time-course NIR-II fluorescence imaging was performed to monitor the *in vivo* biodistribution of NR@Min-23@AuNCs at 0.5, 2, 4, 6, 8 and 10 h post-injection (*p.i.*). After that, the mice were euthanized with major organs and tumors being harvested for *ex vivo* imaging. On the other hand, ~50  $\mu$ L of blood were collected retro-orbitally from the mice at 5, 25, 50, 350, 840, and 2700 min *p.i.* to measure the plasma concentration of AuNCs by ICP-MS.

#### *In vivo smartphone-based PDT*

BALB/c mice (6 – 8 weeks old, n = 5 per group, weight = 18 – 22 g) were used for the 15-day period experiment. The mice were inoculated with 4T1 cells on day 0 and weighed every 2 days and tumor size was measured every 2 days from day 1 to day 14. Once the tumors became palpable (~70 mm<sup>3</sup> in volume) on day 5, the mice were divided into 6 groups of 5 mice per group and treated

every 3 days till day 14, respectively, with (I) 200  $\mu$ L of saline (control), (II) 200  $\mu$ L of NR@Min-23@AuNCs (6.6 mg/Kg), (III) 10  $\mu$ L of NR (1.5 mg/Kg), (IV) 10  $\mu$ L of NR (1.5 mg/Kg) + 2 $\times$ irradiation, (V) 200  $\mu$ L of “full-load” NR@Min-23@AuNCs (6.6 mg/Kg) + 2 $\times$ irradiation, and (VI) 200  $\mu$ L of NR@Min-23@AuNCs (6.6 mg/Kg) + 2 $\times$ irradiation. “2 $\times$ irradiation” represents 60-min smartphone’s torch irradiation, which was performed at  $\sim$ 4 h *p.i.* after anesthesia. Only the tumor site was exposed to 2 $\times$ irradiation, and the rest of mouse body was shielded from the light with a non-transparent film. When the mice were euthanized on day 15, their tumor tissues along with major organs (*e.g.*, heart, liver, spleen, lung, kidney, stomach and brain) were collected for hematoxylin and eosin (H&E), Ki-67 immunohistochemistry staining and TUNEL assay.

**Table S1.** Comparison of typical fluorescence properties (emission  $\lambda_{em}$  center, quantum yield  $\Phi_f$ , emission FWHM, synthesis time) of typical water-soluble NIR-II-emitting AuNCs.

Ligand	$\lambda_{em}$ center (nm) (single/dual)	$\Phi$ (%)	FWHM (nm)	Time (h)	Ref.
MHA/HDT <sup>a)</sup>	932, 1075 (dual)	6.1	~150, ~220	8	46
Glutathione	~850, ~1050 (dual)	0.67	~238, ~212	24	13
MHA/TDT <sup>b)</sup>	~930, ~1033 (dual)	~6	~177.9, ~174.3	8	45
LA-sulfobetaine	~1000 (single)	0.6	289.5	$\geq 8$	47
Min-23	1000 (single)	0.21	198.9	~0.016	This work

<sup>a)</sup>Mercaptohexanoic acid (MHA), hexa(ethylene glycol)dithiol; <sup>b)</sup>Tetra(ethyleneglycol)dithiol (TDT).

**Table S2.** Characterization of the three samples prepared in this work.

Samples	Mean $D_h \pm SD$ (nm)	PDI	Mean ZP $\pm SD$ (mV)	Crosslinker loading (DBCO-PEG4/AuNC ratio)	Drug loading (NR/AuNC ratio)
Min-23@AuNCs	$3.7 \pm 1.4$	0.15	$12.9 \pm 2.5$	—	—
NR@Min-23@AuNCs	$6.4 \pm 1.4$	0.05	$10.6 \pm 5.3$	4.1/1	2.5/1
“full-load” NR@Min-23@AuNCs	$11.5 \pm 2.5$	0.05	$1.5 \pm 3.5$	8.4/1	5.3/1

Abbreviations:  $D_h$ , hydrodynamic diameter; PDI, polydispersity index; ZP, zeta potential.

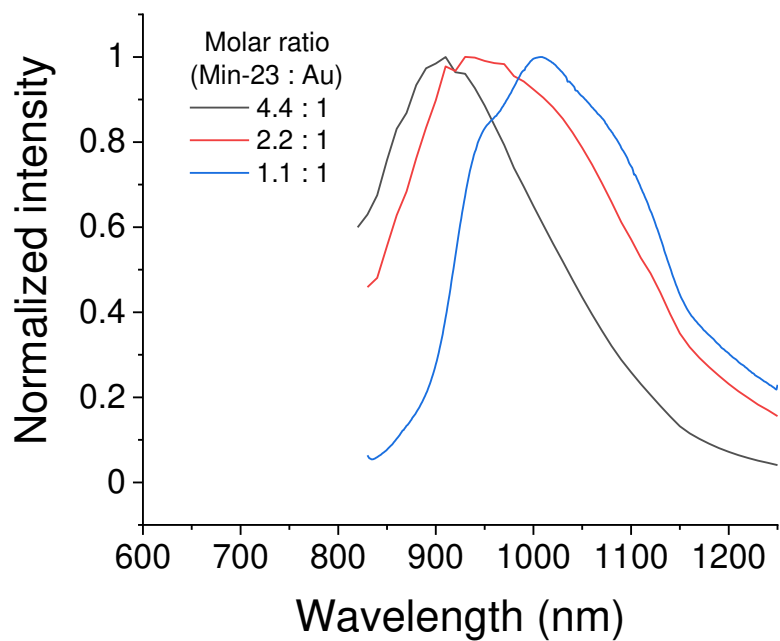


**Fig. S1** Fluorescence spectra of Min-23@AuNCs with different molar ratios of Min-23 to Au ions (1.1 : 1, 2.2 : 1, and 4.4 : 1).

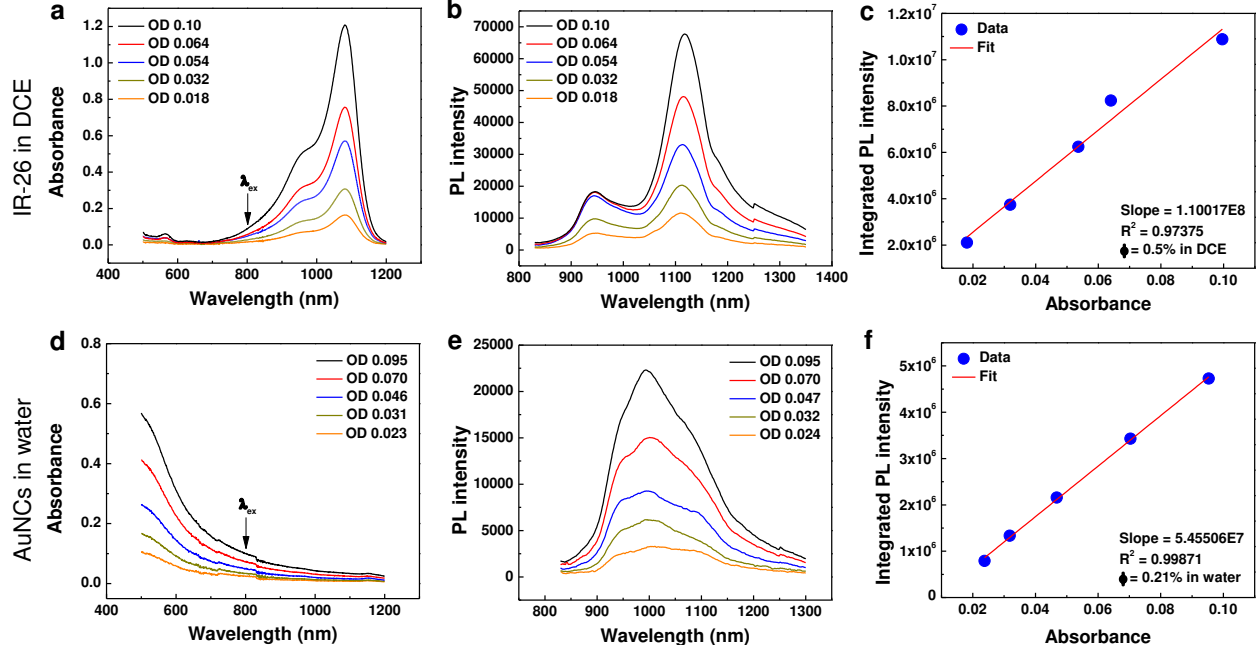


**Fig. S2** Quantum yield calculation: a) UV/Vis/NIR absorption spectra of IR-26 solutions in DCE with a set of concentrations as the reference. b) NIR-II fluorescence spectra of IR-26 solutions shown in (a) under the 808-nm-laser excitation at RT. c) Integrated NIR-II fluorescence intensity of IR-26 solutions plotted as a function of the absorbance at 808 nm acquired from the data in (a) and (b), where the data points are fitted into a linear function with a slope of  $1.1002 \times 10^8$ . d) UV-Vis-NIR absorption spectra of aqueous solutions of Min-23@AuNCs with a set of concentrations. e) NIR-II fluorescence spectra of aqueous solutions of Min-23@AuNCs shown in (d) under the excitation of 808 nm at RT. f) Integrated photoluminescence (PL) intensity of aqueous solutions of Min-23@AuNCs plotted as a function of the absorbance at 808 nm acquired from the data in (d) and (e), where data points are fitted into a linear function with a slope of  $5.4551 \times 10^7$ . The quantum yield of Min-23@AuNCs is 0.21%, calculated using the following equation:

$$\Phi_{\text{Au}} = \Phi_{\text{Ref}} \left( \frac{\text{Slope}_{\text{Au}}}{\text{Slope}_{\text{Ref}}} \right) \left( \frac{\eta_{\text{Au}}}{\eta_{\text{Ref}}} \right)^2$$

Where the subscripts Ref (reference) and Au denote IR-26 and Min-23@AuNCs, respectively;  $\Phi$  is the quantum yield ( $\Phi_{\text{Ref}} = 0.5\%$ ); Slope is the gradient from the plot of integrated PL intensity vs absorbance;  $\eta$  is the refractive index of the solvent (DCE for IR-26, water for Min-23@AuNCs).

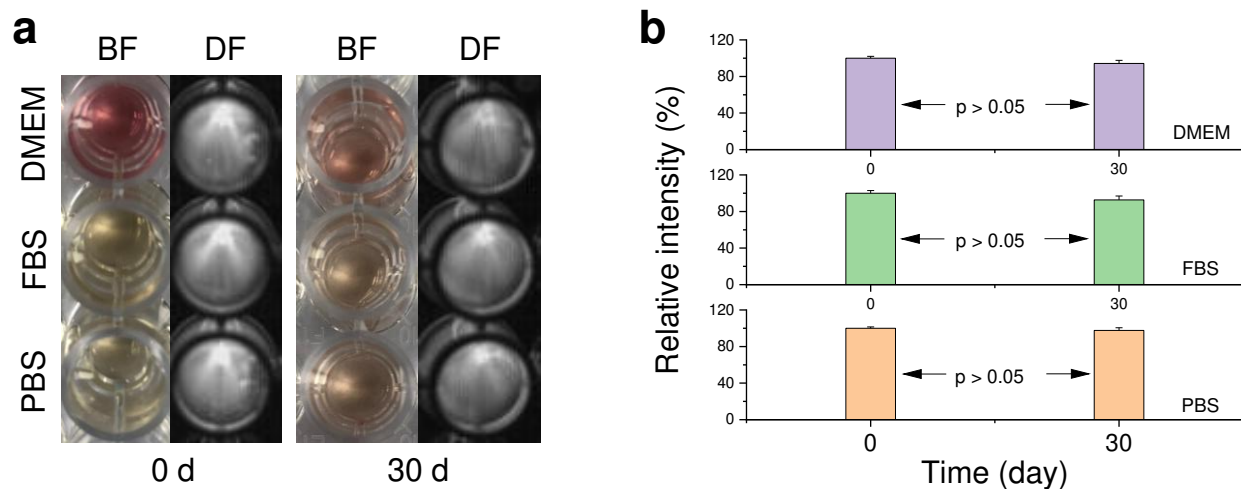


**Fig. S3** a) Bright-field (BF) and dark-field (FL) images of Min-23@AuNCs dispersed in DMEM, FBS and PBS on days 0 and 30 of a 30-day storage. BF images were captured with the smartphone, while DF images were captured with the NIR-II *in vivo* imaging system ( $\lambda_{ex} = 808$  nm, 150 mW/cm<sup>2</sup>, 100 ms exposure, long-pass filter: 1000 nm). b) Corresponding relative intensity of Min-23@AuNCs in the buffers. The data are compared using Student's t-test.

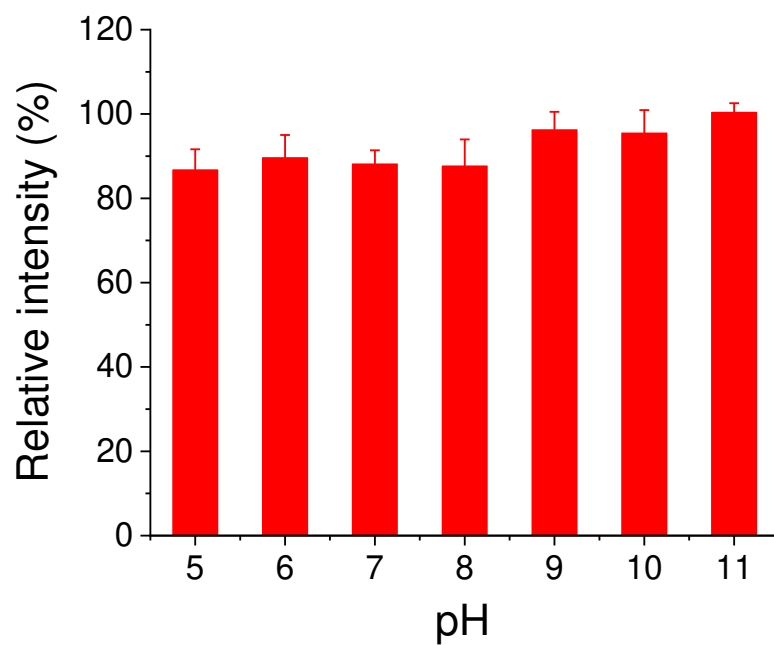


**Fig. S4** Effect of pH on the relative fluorescence intensity of Min-23@AuNCs ( $\lambda_{\text{ex}} = 808 \text{ nm}$ ,  $\lambda_{\text{em}} = 1000 \text{ nm}$ ).

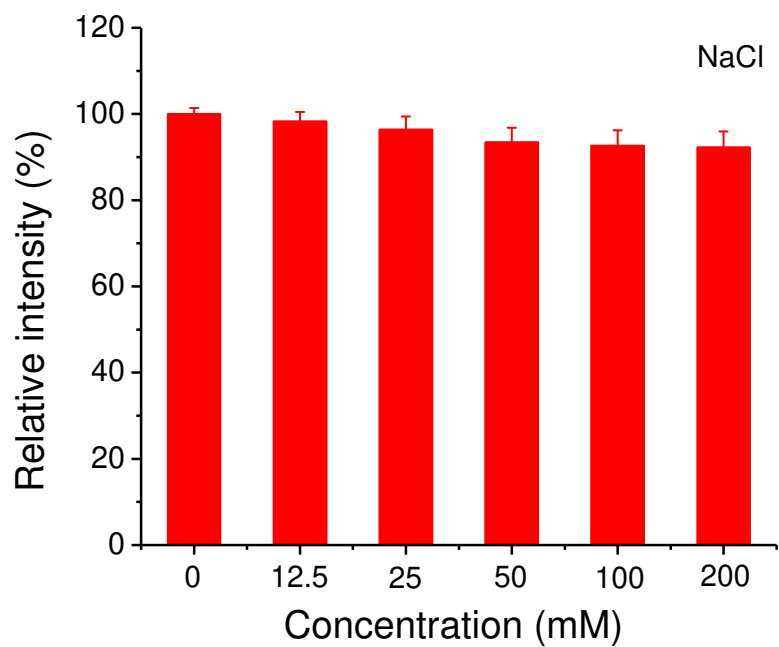


**Fig. S5** Effect of NaCl on the relative fluorescence intensity of Min-23@AuNCs as a function of concentration (*e.g.*, 0, 12.5, 25, 50, 100, and 200 mM) ( $\lambda_{\text{ex}} = 808$  nm,  $\lambda_{\text{em}} = 1000$  nm).

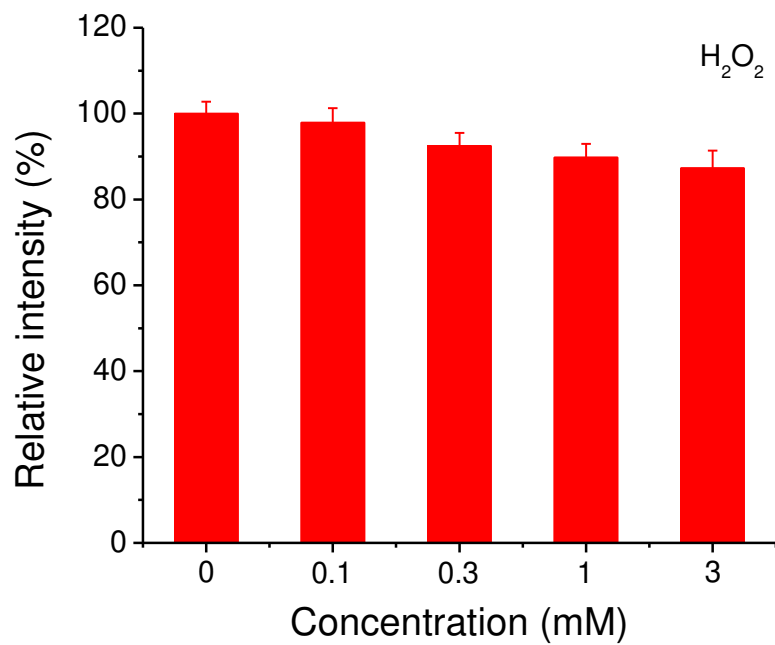


**Fig. S6** Effect of H<sub>2</sub>O<sub>2</sub> on the relative fluorescence intensity of Min-23@AuNCs as a function of concentration (*e.g.*, 0, 0.1, 0.3, 1, and 3 mM) ( $\lambda_{\text{ex}} = 808$  nm,  $\lambda_{\text{em}} = 1000$  nm).

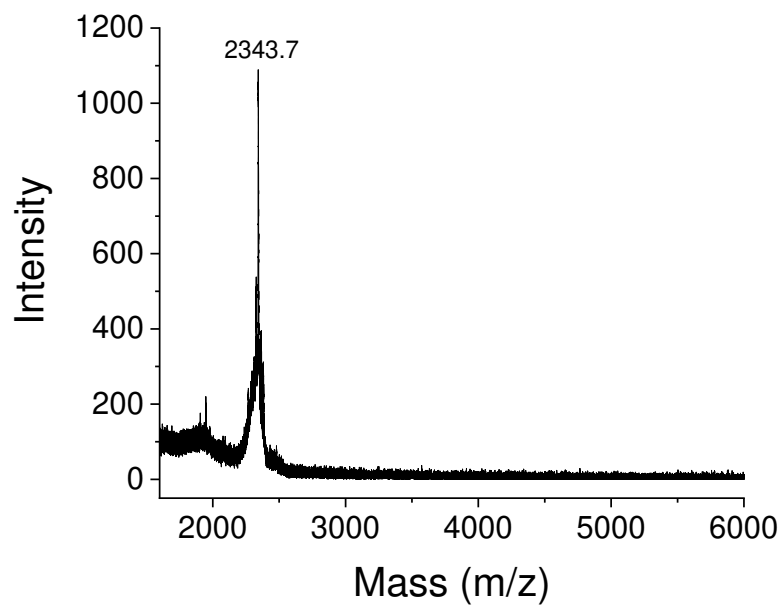


**Fig. S7** MALDI-TOF MS spectrum of Min-23.

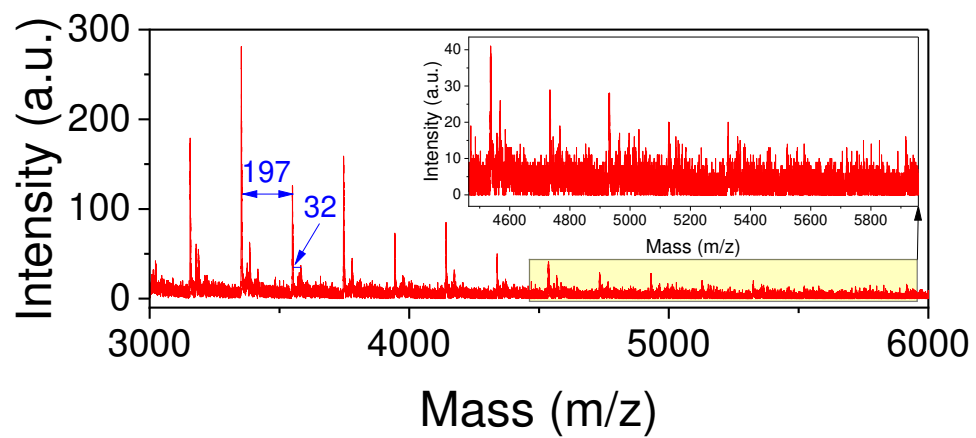


**Fig. S8** MALDI-TOF MS spectrum of Min-23@AuNCs.

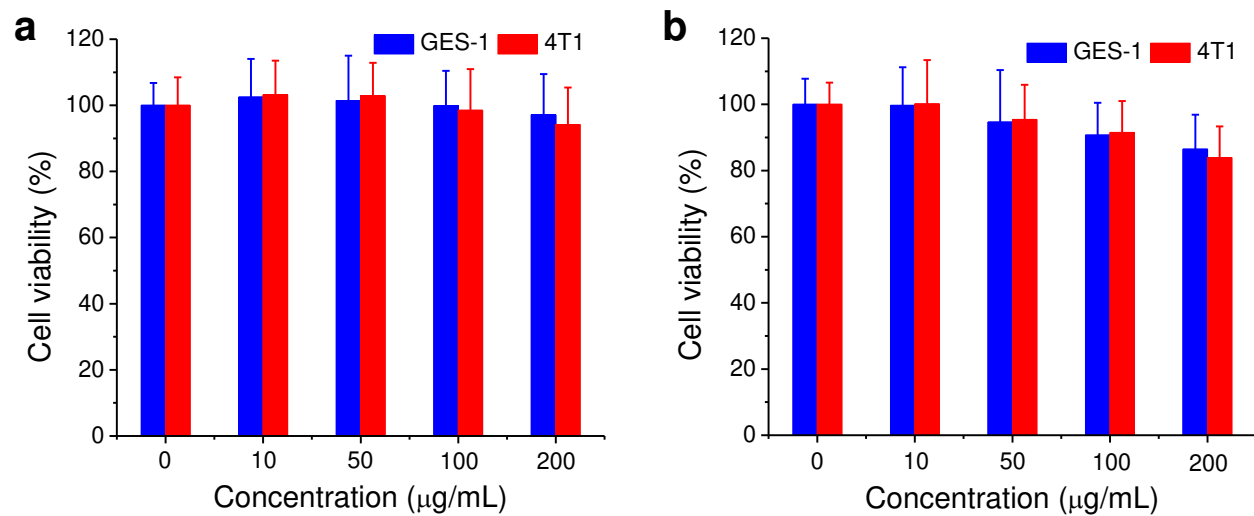


**Fig. S9** Viability of GES-1 and 4T1 cells incubated with a) Min-23@AuNCs and b) NR@Min-23@AuNCs ranging from 0 to 200 µg/mL for 24 h, measured by MTT assay. The data are expressed as the mean  $\pm$  s.d. for  $n = 3$  per concentration.

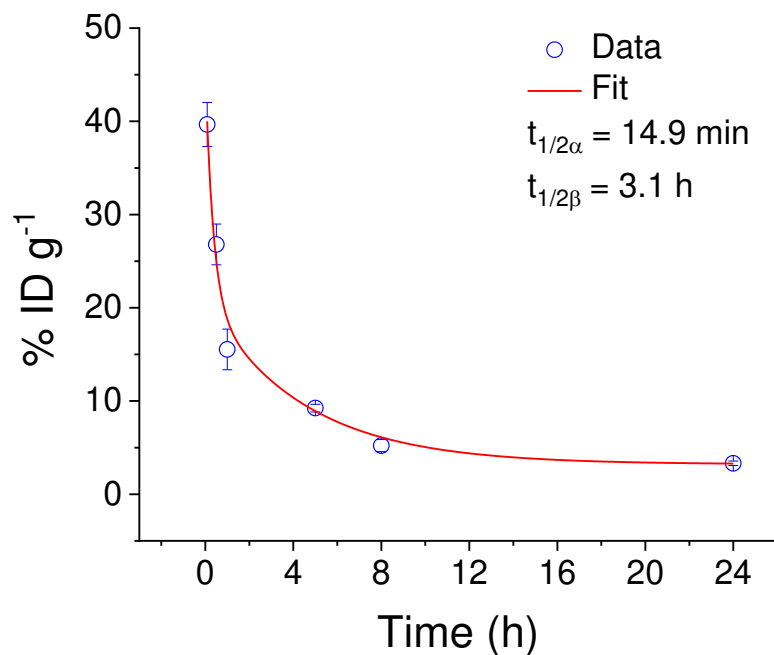


**Fig. S10** Plasma pharmacokinetic profile of Min-23@AuNCs in mice over a time span of 24 h after *i.v.* injection, which is well fitted ( $R^2 = 0.98$ ) to a bi-exponential decay function, giving a distribution half-life ( $t_{1/2\alpha}$ ) of 14.9 min and an elimination half-life ( $t_{1/2\beta}$ ) of 3.1 h.

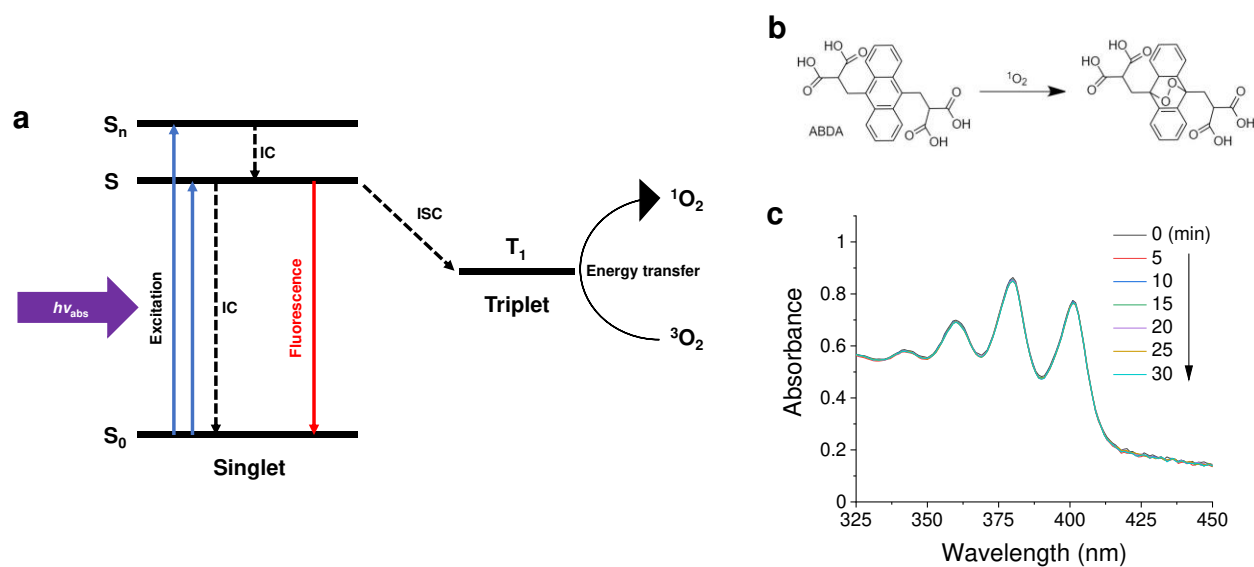


**Fig. S11** a) Energy level diagram of AuNC for photosensitization. b) Schematic illustration of oxidation of ABDA by  $^1\text{O}_2$ . c) Time-lapse absorption spectra of ABDA ( $50 \mu\text{M}$ ) mixed with Min-23@AuNCs at  $100 \mu\text{g/mL}$  in  $\text{D}_2\text{O}$  at varying time points under green laser irradiation ( $532 \text{ nm}$ , fluence rate:  $100 \text{ mW/cm}^2$ ).

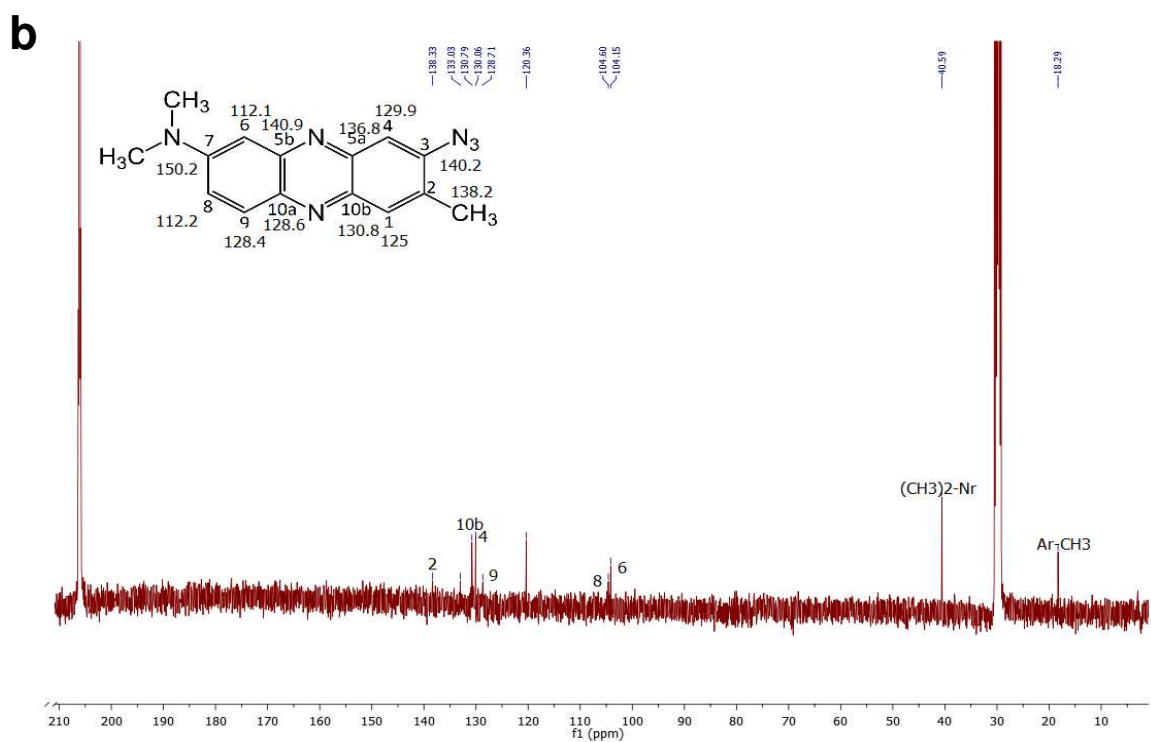
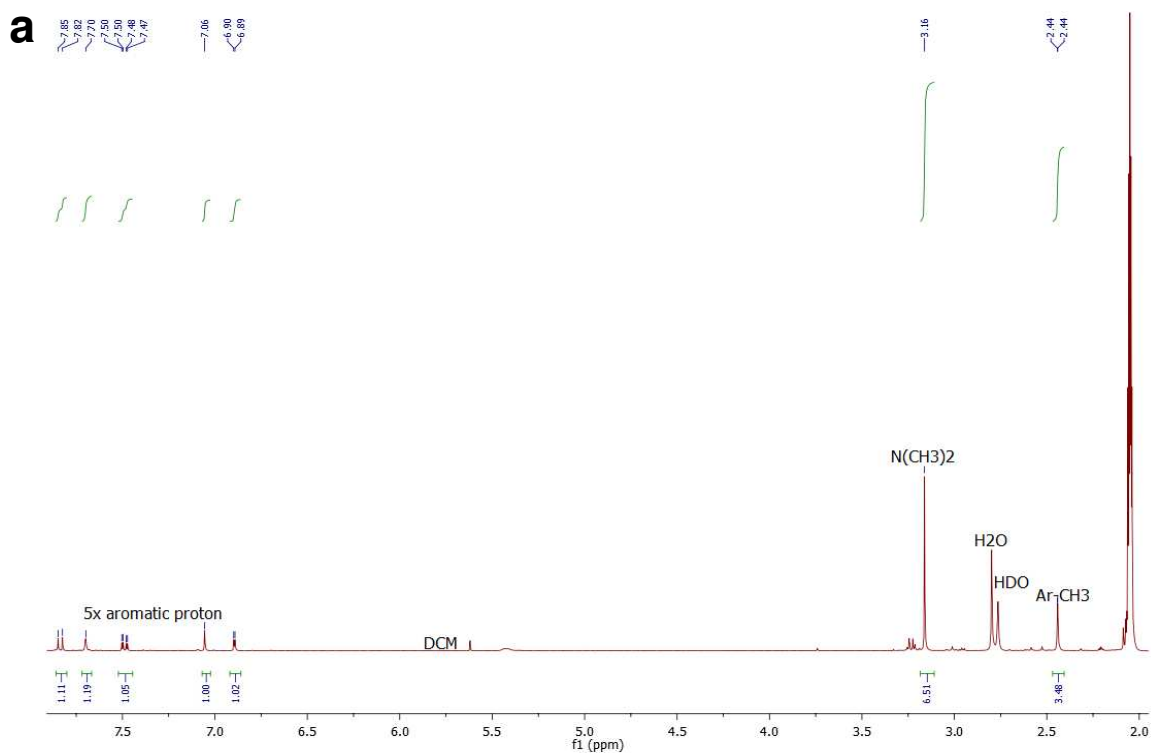


**Fig. S12** a)  $^1\text{H}$  and b)  $^{13}\text{C}$  NMR spectra of 2-azido-3-methyl-8-(*N,N*-dimethyl-amino)phenazine) in acetone- $\text{d}_6$  (the strong peaks at  $\sim 2.05$  ppm in the  $^1\text{H}$  NMR spectrum and peaks at  $\sim 30$  and  $\sim 207$  ppm in  $^{13}\text{C}$  NMR spectrum are the  $\text{CD}_3\text{CN}$  solvent residue peaks).

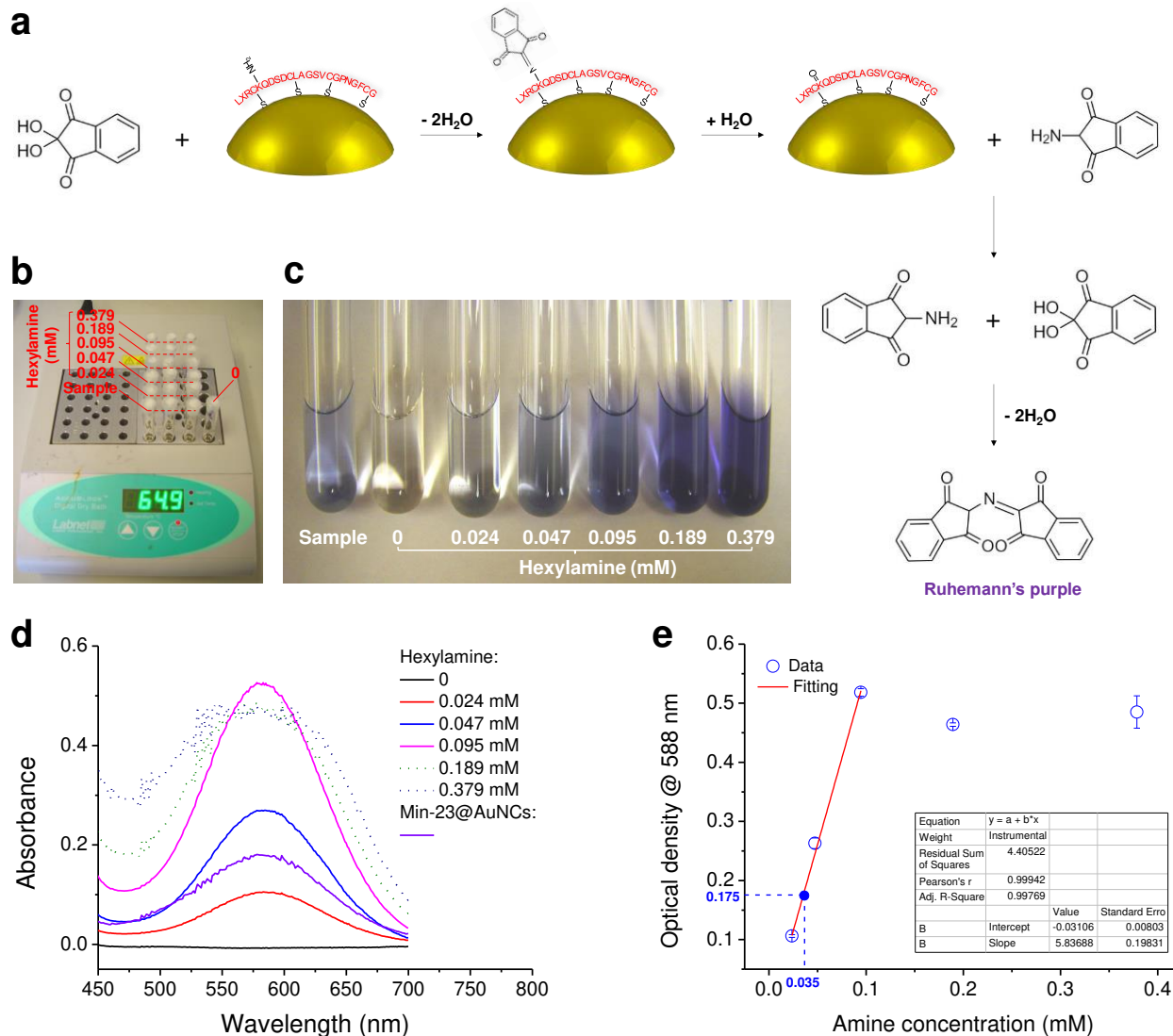


**Fig. S13** Quantitative estimation of primary amine groups on the surface of Min-23@AuNCs through ninhydrin assay. a) Schematic illustration of reaction mechanism between ninhydrin and the amine groups in Min-23. b) Photograph of test tubes containing ninhydrin solutions mixed with Min-23@AuNCs (sample) or hexylamine standards placed in a dry-bath incubator. c) Photograph and d) UV-vis spectra of dark-purple solutions, indicating the formation of Ruhemann's purple (RP). Note that the saturated curves (dot lines) observed at high hexylamine concentrations (0.189 and 0.279 mM) are flattened, where the absorbance is lower than what it should be. e) Calibration curve of RP. Note that the two outliers of optical density (OD) at 588 nm wavelength were omitted from the fitting, and the linear fit was perfect with  $R^2 > 0.99$ . The OD value can be translated into the concentration of amino groups. The data are expressed as the mean  $\pm$  s.d. for  $n = 3$  per concentration.

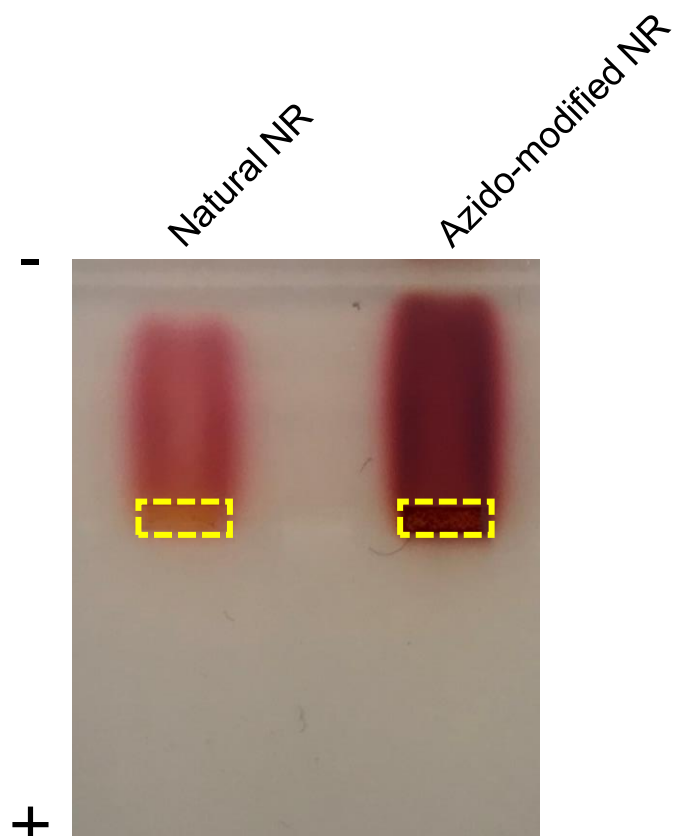


**Fig. S14** Agarose gel electrophoresis image of natural NR and azido-modified NR.

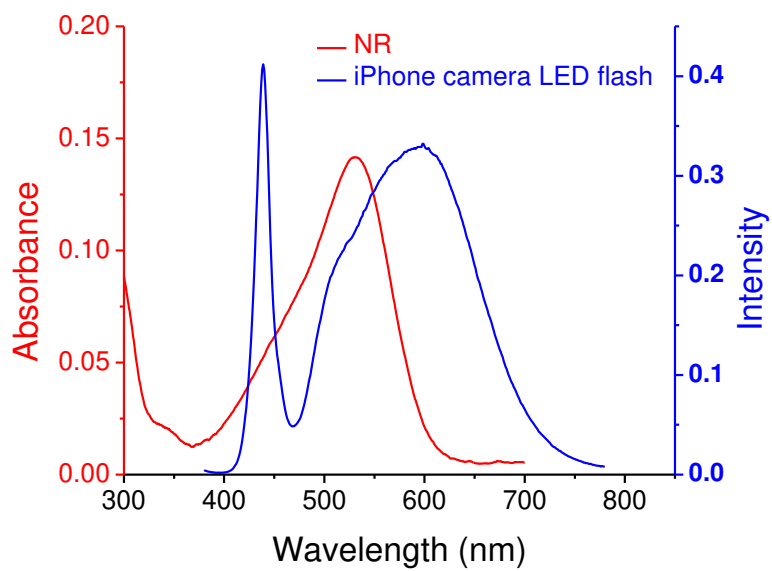


**Fig. S15** Red line: UV-vis absorption of NR. Blue line: Spectrographic analysis of iPhone's flashlight.

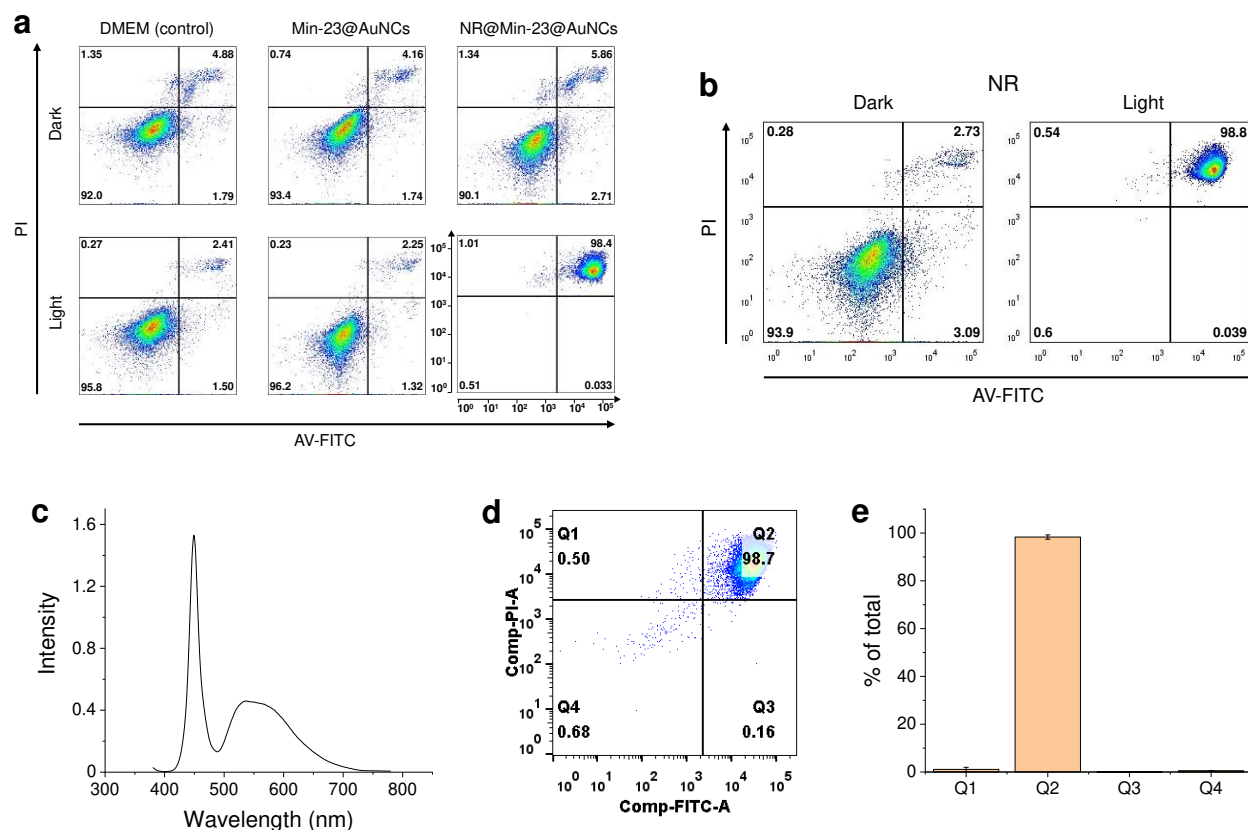


**Fig. S16** Representative dot-plots of Annexin V-FITC/PI flow cytometric analysis on 4T1 cells after 0.5-h incubation with a) DMEM, 100  $\mu\text{g}/\text{mL}$  Min-23@AuNCs or 100  $\mu\text{g}/\text{mL}$  NR@Min-23@AuNCs (equivalent to  $\sim 15$   $\mu\text{g}/\text{mL}$  NR) or b) 15  $\mu\text{g}/\text{mL}$  NR with or without smartphone's torch irradiation (fluence rate: 8  $\text{mW}/\text{cm}^2$ ; radiant exposure: 14.4  $\text{J}/\text{cm}^2$ ). Quadrants Q1 (upper left), Q2 (upper right) and Q3 (lower right), and Q4 (lower left) correspond to necrotic, late and early apoptotic, and viable cells, respectively. c) Spectrographic analysis of a broadband LED lamp. d) Representative dot-plot of Annexin V-FITC/PI flow cytometric analysis on 4T1 cells exposed to the combined use of 100  $\mu\text{g}/\text{mL}$  NR@Min-23@AuNCs and the broadband LED irradiation (fluence rate: 96  $\text{mW}/\text{cm}^2$ ; radiant exposure: 172.8  $\text{J}/\text{cm}^2$ ). e) Percentage of viable, both apoptotic (late and early), and necrotic cells.

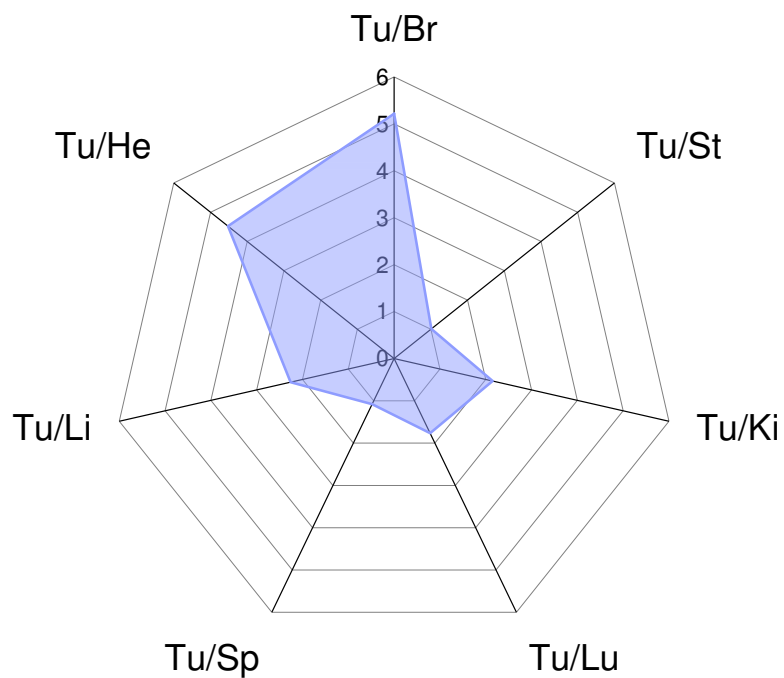


**Fig. S17** Signal ratio of average intensity of tumor to various organs. Abbreviation: He, heart; Li, liver; Sp, spleen; Lu, lung; Ki, kidney; St, stomach; Br, brain; Tu, tumor.

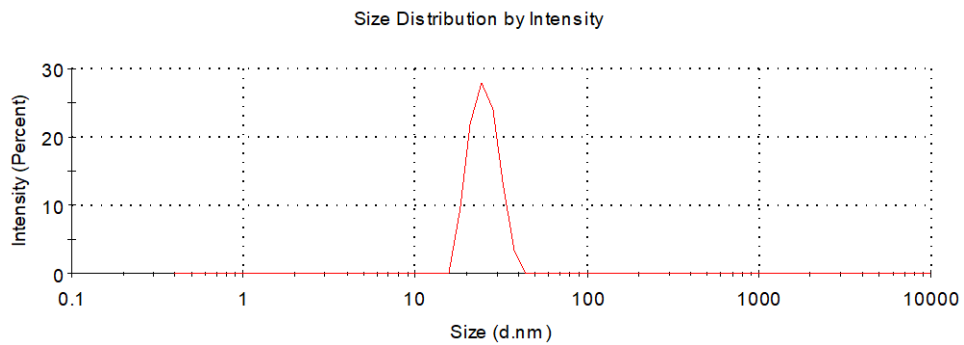


**Fig. S18** Hydrodynamic diameter of NR@Min-23@AuNCs ( $D_h = 25.5$  nm) dispersed in DMEM plus 20% FBS, measured by DLS.

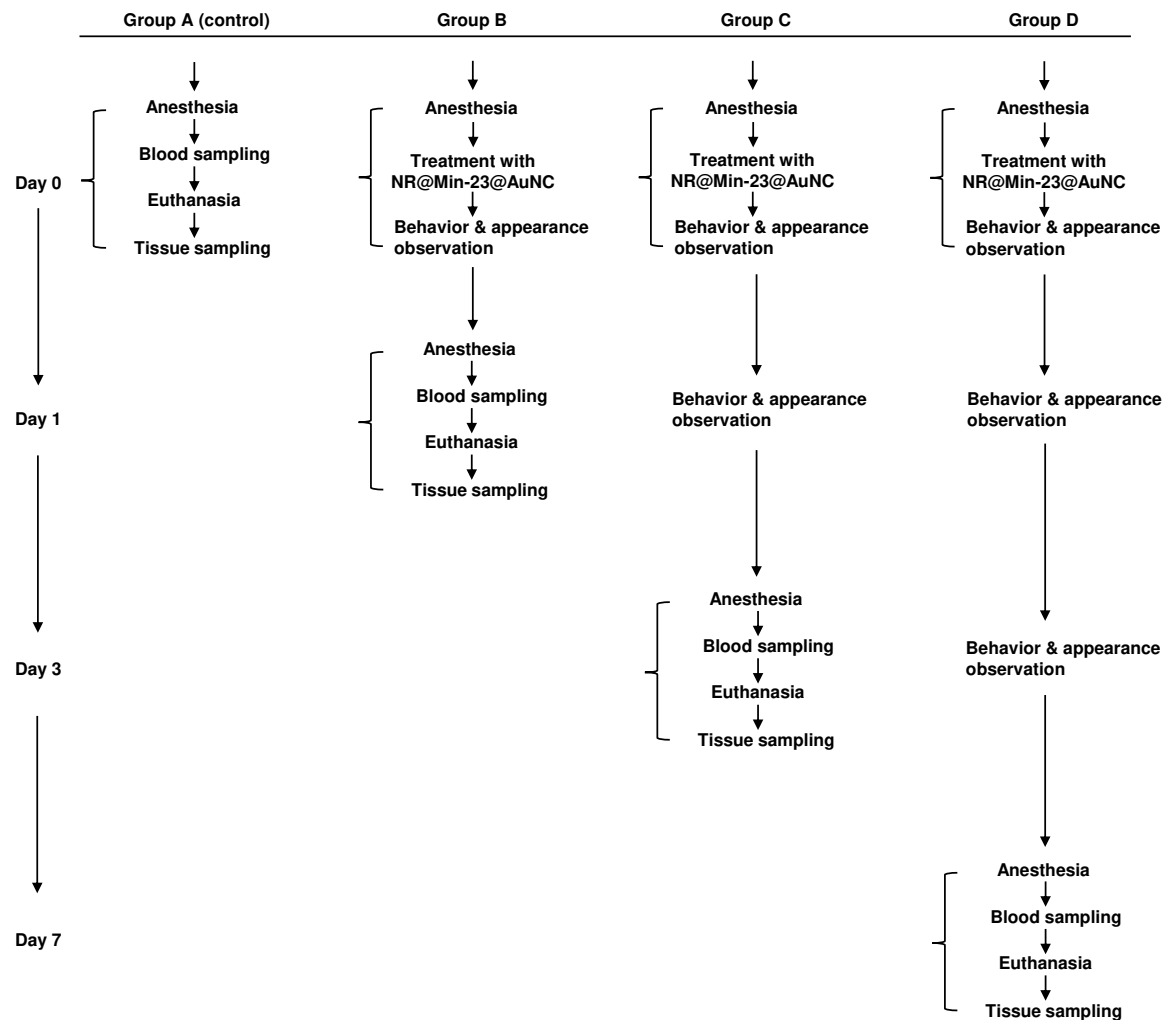


**Fig. S19** Flowchart and timeline of the experimental design. Group A (control): non-treated mice undergo anesthesia and blood sampling before euthanasia for tissue sampling on Day 0. Groups B to D: mice treated with NR@Min-23@AuNCs (200  $\mu$ L, 6.6 mg/Kg) on Day 0 undergo all procedures (*i.e.*, anesthesia, blood sampling, euthanasia and tissue sampling) on Day 1 (Group B), Day 3 (Group C) or Day 7 (Group D). The mouse appearance and behavior are monitored during the experiment period.

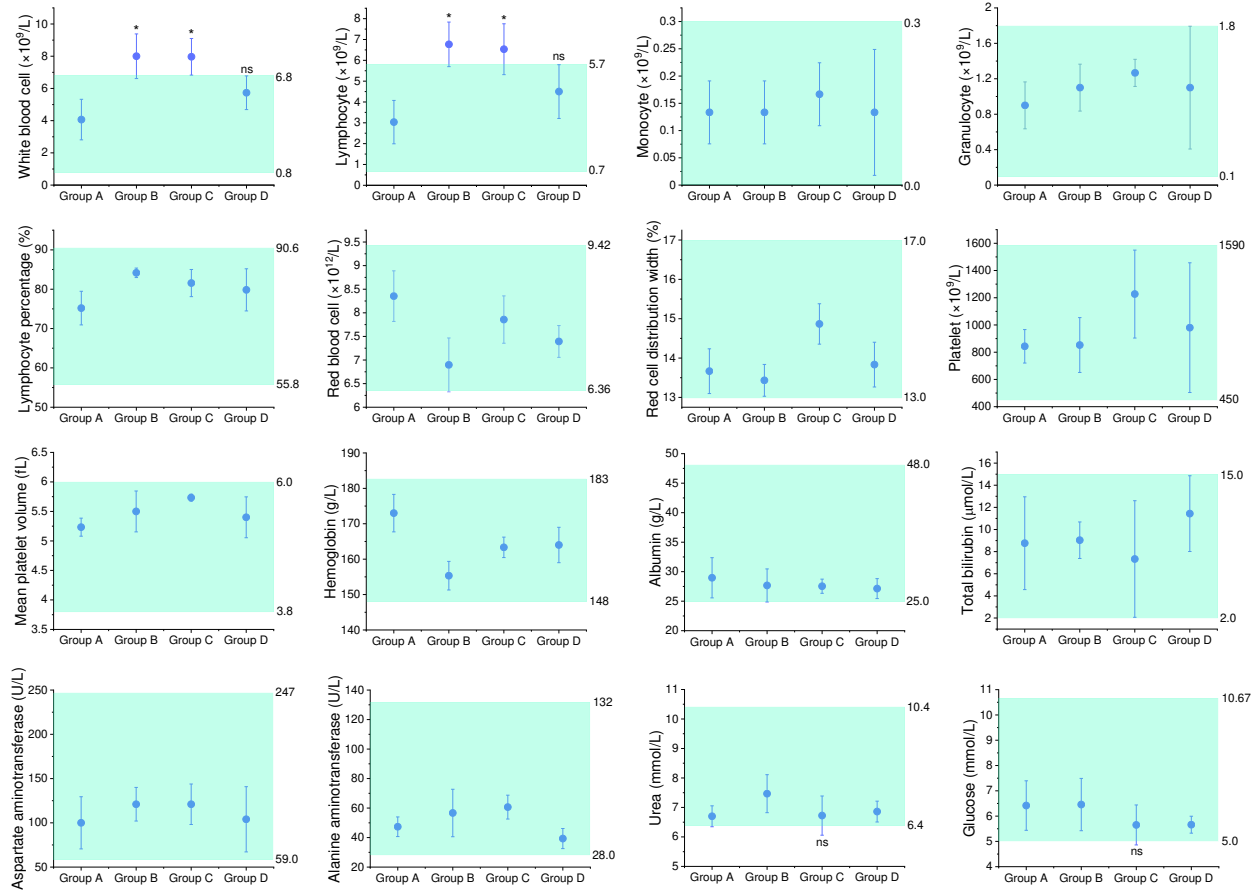


**Fig. S20** Blood test results of control (Group A) and experimental mice (Groups B, C, and D). Blood routine and biochemical indicators include: white blood cell, lymphocyte, monocyte, and granulocyte (Row 1); lymphocyte percentage, red blood cell, red cell distribution width, and platelet (Row 2); mean platelet volume, hemoglobin, albumin, and total bilirubin (Row 3); aspartate aminotransferase, alanine aminotransferase, urea, and glucose (Row 4). The green shadows represent normal reference ranges provided by the analyzers. The data are expressed as the mean  $\pm$  s.d.; ns =  $p > 0.05$  (unpaired two-tailed Student's t-test versus Group A); \* =  $p < 0.05$  (unpaired two-tailed Student's t-test versus Group A).

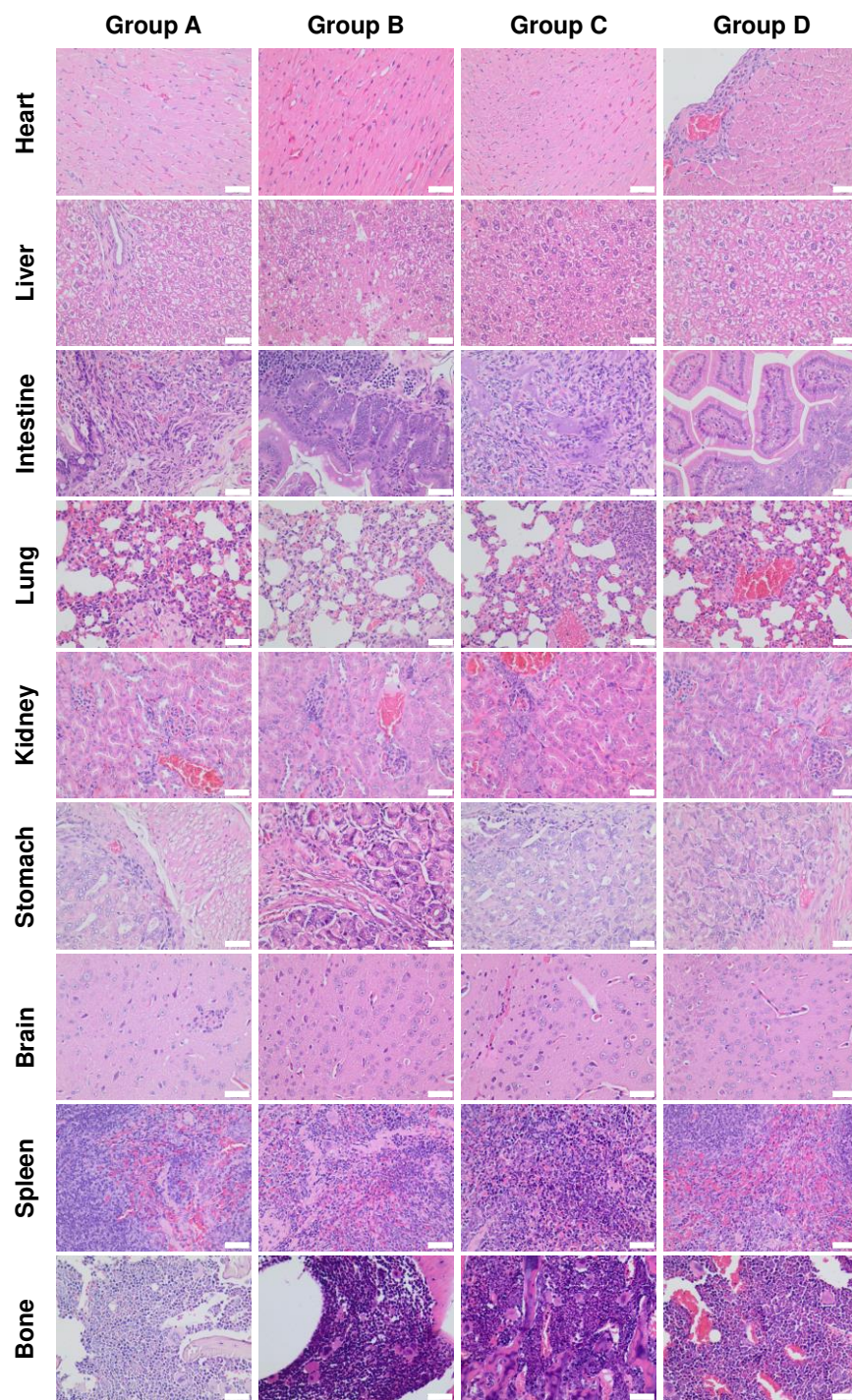


**Fig. S21** H&E staining of major organs and tissues (*e.g.*, heart, liver, intestine, lung, kidney, stomach, brain, spleen, bone, *etc.*) collected from control (Group A) and experimental mice (Groups B, C, and D) at time of sacrifice. Scale bar, 20  $\mu$ m.

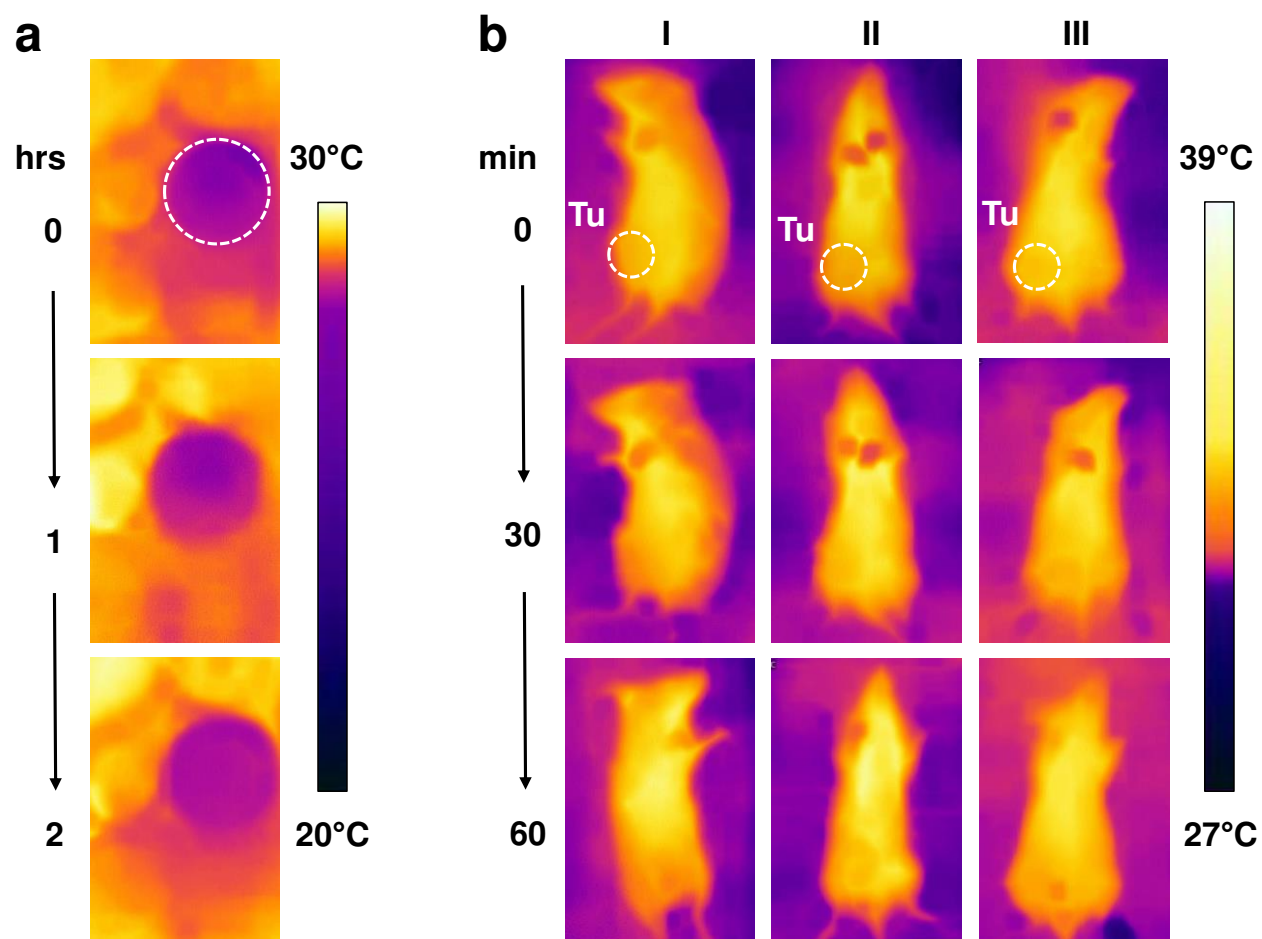


**Fig. S22** Measurements of heat generation *in vitro* and *in vivo*. a) Time-lapse thermal imaging of the NR@Min-23@AuNC solution placed in a well (outlined by a white dash circle) of a 6-well culture plate under continuous irradiation with the smartphone's torch (fluence rate:  $8 \text{ mW/cm}^2$ ). Images are shown at exposure time = 0, 1 and 2 h. b) Time-lapse thermal imaging of 4T1 tumor-bearing mice receiving (I) no treatment, (II) irradiation alone, or (III) irradiation plus *i.v.* injection of  $200 \mu\text{L}$  NR@Min-23@AuNCs ( $6.6 \text{ mg/Kg}$ ). White dash circles denote tumor (Tu) regions. The mice in Groups II and III are irradiated under the condition identical to that used in (a). The typical images are shown at exposure time = 0, 30 and 60 min.

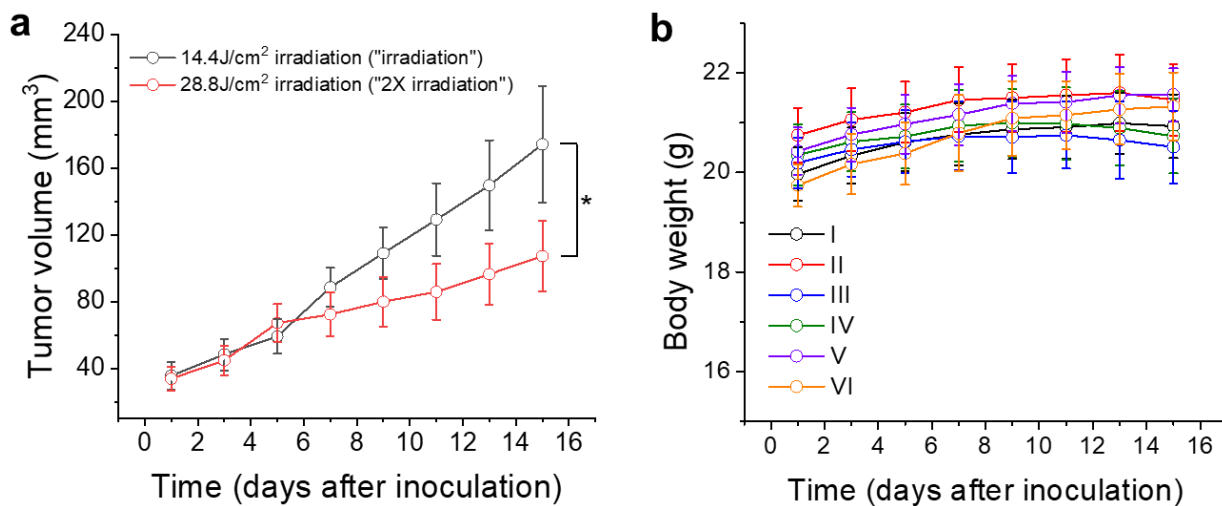


**Fig. S23** a) Tumor growth curves of NR@Min-23@AuNCs-treated mice subjected to 14.4 J/cm<sup>2</sup> irradiation ("the irradiation") or 28.8 J/cm<sup>2</sup> irradiation ("2× irradiation") with smartphone's torch. The data are expressed as the mean ± s.d. for n = 5 per treatment group and compared using one-way ANOVA test. Significant difference is indicated by asterisks: \* = p < 0.05. b) Average body weight of mice in different groups during the course of the experiment.

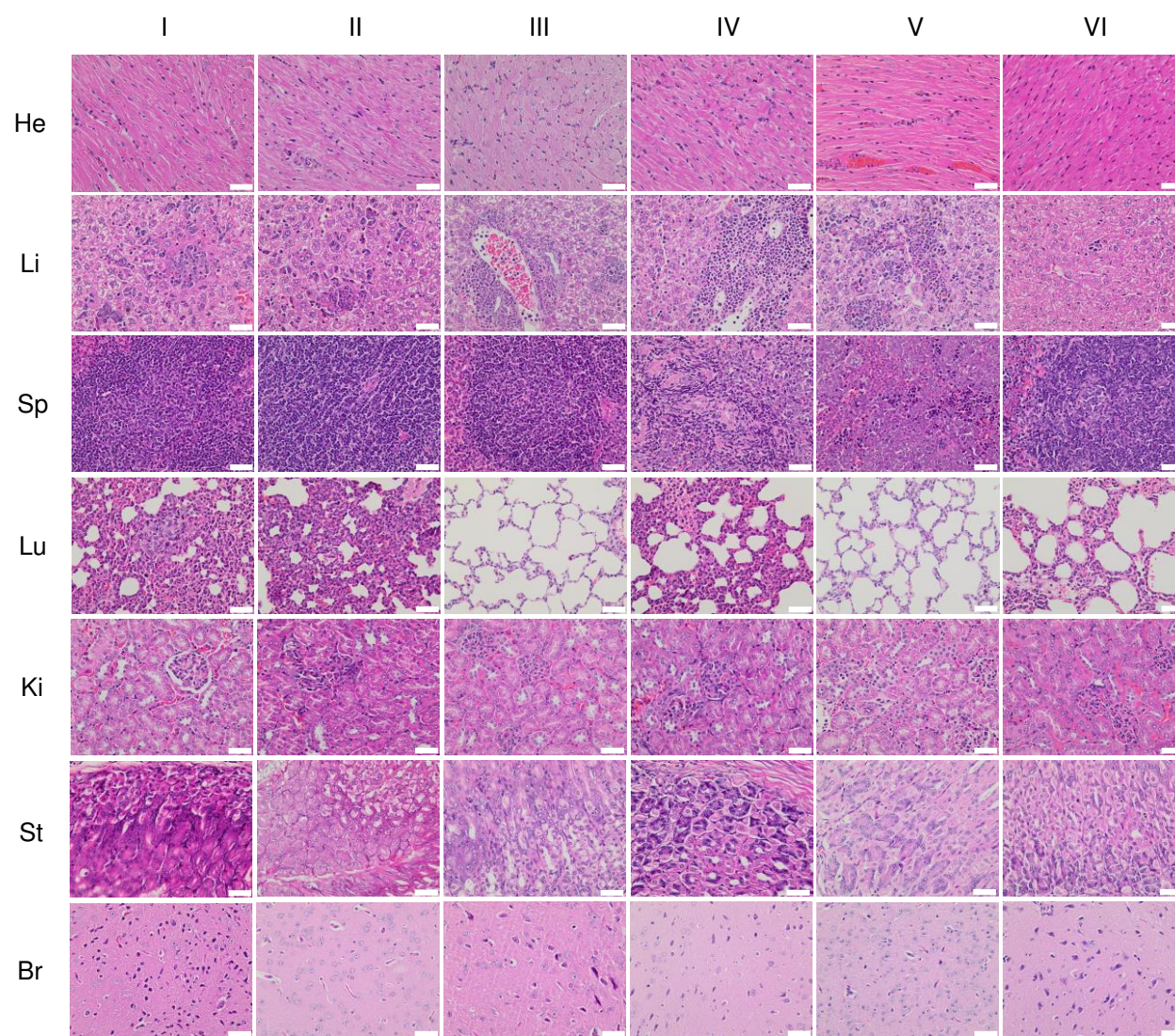


**Fig. S24** H&E staining of major organs harvested from mice at time of sacrifice. The mice are randomly divided into 6 groups and treated with (I) saline, (II) NR@Min-23@AuNCs, (III) NR, (IV) NR + 2×irradiation, (V) “full-load” NR@Min-23@AuNCs + 2×irradiation and (VI) NR@Min-23@AuNCs + 2×irradiation, respectively. “2×irradiation” represents 60 min smartphone’s torch irradiation (fluence rate: 8.0 mW/cm<sup>2</sup>; radiant exposure: 28.8 J/cm<sup>2</sup>). Abbreviation: He, heart; Li, liver; Sp, spleen; Lu, lung; Ki, kidney; St, stomach; Br, brain. Scale bar, 20 μm.

## Supplementary references

1. Kresse, G., and Hafner, J., *Physical Review B* (1993) **47** (1), 558
2. Kresse, G., *et al.*, *Physical Review B* (1994) **50** (18), 13181
3. Kresse, G., and Furthmüller, J., *Physical Review B* (1996) **54** (16), 11169
4. Kresse, G., and Furthmüller, J., *Computational Materials Science* (1996) **6** (1), 15
5. Blöchl, P. E., *Physical Review B* (1994) **50** (24), 17953
6. Kresse, G., and Joubert, D., *Physical Review B* (1999) **59** (3), 1758
7. Grimme, S., *Journal of Computational Chemistry* (2006) **27** (15), 1787
8. Sun, J., *et al.*, *Physical Review Letters* (2015) **115** (3), 036402
9. Sheppard, D., *et al.*, *The Journal of Chemical Physics* (2008) **128** (13), 134106
10. Hestenes, M. R., and Stiefel, E., *Methods of Conjugate Gradients for Solving Linear Systems*. NBS Washington, DC: 1952
11. Mermin, N. D., *Physical Review* (1965) **137** (5A), A1441
12. Henkelman, G., *et al.*, *Computational Materials Science* (2006) **36** (3), 354
13. Sanville, E., *et al.*, *Journal of Computational Chemistry* (2007) **28** (5), 899
14. Tang, W., *et al.*, *Journal of Physics: Condensed Matter* (2009) **21** (8), 084204
15. Momma, K., and Izumi, F., *Journal of Applied Crystallography* (2011) **44** (6), 1272
16. Billy, D., *Chemical Communications* (2017) **53** (77), 10715
17. McGuill, M. W., *et al.*, *ILAR Journal* (1989)**31**(4), 5
18. Pulaski, B. A., and Ostrand - Rosenberg, S., *Current Protocols in Immunology* (2000) **39** (1), 20.2. 1